Inorganic Chemistry

Article

pubs.acs.org/IC

Revisit of Pressure-Induced Phase Transition in PbSe: Crystal Structure, and Thermoelastic and Electrical Properties

Shanmin Wang,*[,†,‡,§] Chengpeng Zang,[†,∥] Yongkun Wang,[‡] Liping Wang,[†] Jianzhong Zhang,[§] Christian Childs,[†] Hui Ge,[⊥] Hongwu Xu,[§] Haiyan Chen,[#] Duanwei He,[‡] and Yusheng Zhao*[,†,§]

[†]HiPSEC & Department of Physics, University of Nevada, Las Vegas, Nevada 89154, United States

[‡]Institute of Atomic & Molecular Physics, Sichuan University, Chengdu 610065, China

[§]Los Alamos National Laboratory, Los Alamos, New Mexico 87545, United States

[∥]Department of Physics, Shanghai Jiao Tong University, Shanghai 200240, China

[⊥]Institute of Coal Chemistry, Chinese Academy of Sciences, Taiyuan, Shanxi 030001, China

[#]Mineral Physics Institute, Stony Brook University, Stony Brook, New York 11794, United States

Supporting Information

ABSTRACT: Lead selenide, PbSe, an important lead chalcogenide semiconductor, has been investigated using *in-situ* high-pressure/high-temperature synchrotron X-ray diffraction and electrical resistivity measurements. For the first time, high-quality X-ray diffraction data were collected for the intermediate orthorhombic PbSe. Combined with *ab initio* calculations, we find a *Cmcm*, InI-type symmetry for the intermediate phase, which is structurally more favorable than the *anti*-GeS-type *Pnma*. At room temperature, the onset of the cubic−orthorhombic transition was observed at ∼3.5 GPa with a ∼3.4% volume reduction. At an elevated temperature of 1000 K, the reversed orthorhombic-to-cubic transition was observed at 6.12 GPa, indicating a positive Clapeyron slope for the phase boundary. Interestingly, phase-transition induced elastic softening in PbSe was also observed, which can be mainly attributed to the loosely bonded trigonal prisms along the *b*-axis in the *Cmcm* structure. In a comparison with the cubic phase, orthorhombic PbSe exhibits a large negative pressure dependence of electrical resistivity. In addition, thermoelastic properties of orthorhombic PbSe have been derived from isothermal compression data, such as the temperature derivative of bulk modulus and thermally induced pressure.

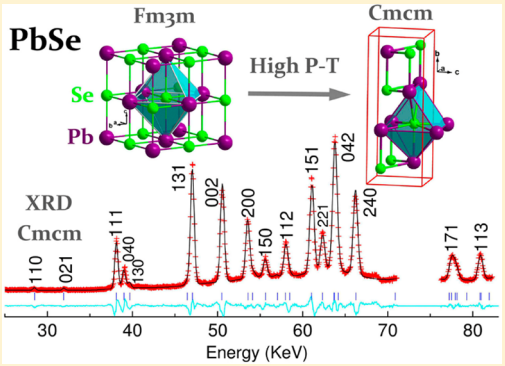

INTRODUCTION

Lead chalcogenides PbX (X = S, Se, and Te), a class of narrow band gap semiconductors, have been extensively studied for several decades because of their promising applications in such diverse fields as electronics and thermoelectrics[1−4] and because of their fundamental importance in condensed-matter physics.[5−9] These compounds, for example, show record high values of thermoelectric figure-of-merit.[3] Anomalous ferroelectric fluctuations[5,6] and giant anharmonic phonon scattering[6,7] have recently been reported in PbX, both of which are associated with the competition between ionic and covalent bonding.[8] At ambient conditions, all three PbX compounds adopt a simple NaCl-type (*B*1) structure. With increasing pressure, the *B*1 structure first transforms into an intermediate orthorhombic phase at 2.1, 4.5, and 6.0 GPa, respectively, in PbS, PbSe, and PbTe, and then transforms into the CsCl-type (*B*2) structure at higher pressures of 21.5, 16.0, and 13.0 GPa.[9,10] Interestingly, the pressure-driven structural transition sequence is correlated with electronic transitions of semiconductor → semiconductor → metal. This is of great interest from a fundamental physics viewpoint, because the associated band gap (E_g) transitions and band gap closures can be simply tuned by the control of pressure and do not involve any compositional changes. Compared with the *B*1 phases of lead chalcogenides, the corresponding high-pressure orthorhombic semiconductors show significantly larger band gaps at the phase transitions.[9] Besides, unlike the more conventional zinc-blende II−VI (e.g., ZnTe) and III−V (e.g., GaN) semiconductors, the *B*1 PbX semiconductors exhibit a number of peculiar electronic properties (ref 11). The E_g of PbSe, for example, decreases with pressure, in contrast to that of GaN.[12,13] These behaviors have been attributed to an occupied Pb 6s valence band in PbX, which leads to strong repulsion at the *L* point between the Pb 6s and anion 3p states.[11,14] Accurate determination of electronic properties of lead chalcogenides under pressure is still challenging both experimentally and theoretically; as a result, they have been the subject of considerable debate and controversy.[2,14−19]

Received: March 15, 2015
Published: May 4, 2015

DOI: 10.1021/acs.inorgchem.5b00591
Inorg. Chem. 2015, 54, 4981−4989

Because of the coupling between structural and electronic transitions, the determination of the structural characteristics at high-pressures is a key to understanding the corresponding electronic properties of PbX compounds. Despite decades of experimental efforts, the crystal structures of orthorhombic PbX are still under debate between two commonly accepted InI-type (*B*33, *Cmcm* (No. 63)) and *anti*-GeS-type (*B*16, *Pnma* (No. 62)) structures, with the latter having a lower symmetry and slight atomic displacements along the *c*-axis. However, it is difficult to distinguish the two structures on the basis of high-pressure angle-dispersive X-ray diffraction because of severe diffraction peak broadening and overlaps.[20−23] A recent study on Sn-doped PbSe even suggested that these two competing structures may co-exist as intermediate orthorhombic phases at high-pressure.[24] Complicating matter further is that a new orthorhombic FeB-type (*B*27, *Pnma* (No. 62)) phase, neither an *anti*-GeS- nor an InI-type structure, has been reported for the intermediate phase of PbTe.[14,25,26]

Among the three PbX chalcogenides, PbS and PbTe have been studied extensively because of their similarity in structure and electronic properties, while the sister compound PbSe has received relatively little attention.[20,24] As a result, many properties important to fundamental physics and technological applications remain unknown and controversial for PbSe. The experimentally determined elastic bulk modulus of orthorhombic PbSe (B_0 = 73 GPa),[10] for example, is more than 135% larger than that obtained from the first-principles calculations (~31 GPa).[17] To date, all those controversies surrounding the orthorhombic phase have yet to be resolved, calling for more rigorous investigation into its structural, elastic, and electronic behaviors. Very recently, we reported the phase-transition induced elastic softening and band gap transition in PbS at high-pressures, based on high-pressure experiments and first-principles calculations.[10] We proposed new mechanisms for the *B*1−*B*33−*B*2 structural transitions involving atomic translation and lattice distortion.[9] In this work, we have extended our study to that of PbSe using *in-situ* high-pressure/high-temperature synchrotron X-ray diffraction and electrical resistance measurements. Combined with first-principles calculations, we present here an extensive investigation on PbSe, including crystal structure, phase stability, thermal equation of state, and thermoelastic and electronic properties.

EXPERIMENTAL AND CALCULATION METHODS

Commercially available high-purity PbSe powders (>99.999%, ~5 μm) were used in the high-pressure (*P*) and high-temperature (*T*) energy-dispersive X-ray diffraction (XRD) experiment, performed in a DIA-type large-volume cubic press at X17B2 beamline of National Synchrotron Light Source (NSLS-I), Brookhaven National Laboratory.[27,28] The sample powders were thoroughly mixed with amorphous boron (~25% volume fraction) to allow the X-rays readily going through the sample without producing additional diffraction peaks. To the best of our knowledge, boron does not react with the titled compound at high pressures and high temperatures. The presence of boron can also effectively suppress the crystal growth, recrystallization, or reorientation under high *P*−*T* conditions, which helps improve the quality of XRD data collected at high temperatures. Before the experiment, the sample and sodium chloride (NaCl) powders were loaded as separate layers into a cylindrical container of *h*BN, 1.5 mm inner diameter and 2.0 mm length, with the latter serving as the internal pressure standard. The pressure was determined using a Decker scale for NaCl,[29] and the temperature was measured by a W5%Re−W26%Re thermocouple. The experimental details are similar to those described in ref 30. We first compressed the pressure cell at room temperature to 9.5 GPa, followed by heating to the maximum temperature of 1000 K and subsequent cooling to 800, 600, 400, and 300 K. To determine the thermal equation of state, the same procedures were repeated several times at progressively lower pressures. For further investigation of phase stability, some measurements were performed at temperatures up to 1200 K at selected pressures. XRD diffraction data were collected on cooling to minimize non-hydrostatic stress built up during the room temperature compression and decompression. The obtained energy-dispersive XRD data were analyzed using Plot85 software to determine the lattice parameters of PbSe. Rietveld and Le Bail analyses were performed using the GSAS software.[31]

In-situ electrical resistance measurement was carried out in a two-stage Kawai-type large-volume apparatus installed at Sichuan University, China.[32] The as-purchased single-crystal samples (>99.999%) were used in the measurement. Hexagonal boron nitride, *h*BN, was used as the pressure-transmitting medium. The experimental setups for the electrical resistance measurement are similar to those described in ref 32. At room temperature, electrical resistance data were collected during both compression and decompression over the pressure range 0−12 GPa. The cell pressure was precalibrated by an *ex-situ* method performed on compression, and the experimental detail can be found elsewhere.[32]

First-principles calculations were performed for PbSe using the generalized gradient approximation (GGA-PBE) implemented in the VASP package.[33] The projector augmented-wave (PAW) and pseudopotential methods were employed with a plane-wave basis-set, which was truncated at the cutoff energy of 400 eV to obtain a 0.2 meV convergence in total energy per atom.[34] There were 7 × 7 × 7 and 7 × 5 × 7 Monkhorst−Pack *k*-point grids used in the calculations of cubic- and orthorhombic-PbSe, respectively. The final energy convergence for electronic steps is in the magnitude of 1 μeV. The force convergence of ionic steps was set to be 10 μeV/Å. The spin−orbital interaction was involved for band structure calculations.

RESULTS AND DISCUSSION

Figure 1 shows selected high-*P*−*T* energy-dispersive XRD patterns of PbSe taken during compression, heating, and decompression. The onset of the cubic → orthorhombic phase transition was observed at ~3.48 GPa during room temperature compression, which is lower than the previously reported value of 4.5 GPa measured in a diamond-anvil cell (DAC) based on the ruby scale.[10,23] The phase fraction of orthorhombic-PbSe increases as pressure increases, and the two phases co-exist up to ~6.70 GPa. Similar to the findings of previous experiments,[21−24] the observed XRD peaks of orthorhombic PbSe in Figure 1 are significantly broadened and overlapped because of non-hydrostatic stress and structural distortion. However, as temperature increases, the diffraction peaks become sharper and more intense (e.g., collected at 9.39 GPa and 1000 K), and they remain sharp after cooling to 300 K. Such data are later used in the structural refinement for the orthorhombic phase. Apparently, at high pressures, orthorhombic-PbSe can be stabilized at temperatures up to 1000 K. Upon decompression at 1000 K, the reverse orthorhombic → cubic phase transition was first observed at the pressure of ~6.12 GPa (see Figure 1). A detailed high-*P*−*T* phase diagram of PbSe is summarized in Figure 2. Clearly, both cubic and orthorhombic phases can co-exist in a broad *P*−*T* range with a positive Clausius−Clapeyron slope and agree well with the case in PbS.[9] It is noted that we found no evidence of the existence of other metastable phases in addition to orthorhombic phase as predicted previously (ref 14).

Due to the combined effects of photon energy and attenuation, the observed diffraction intensities for PbSe in the range 20−40 keV are substantially weaker than the theoretical values (see Figure 1). Therefore, Rietveld analyses

DOI: 10.1021/acs.inorgchem.5b00591
Inorg. Chem. 2015, 54, 4981−4989

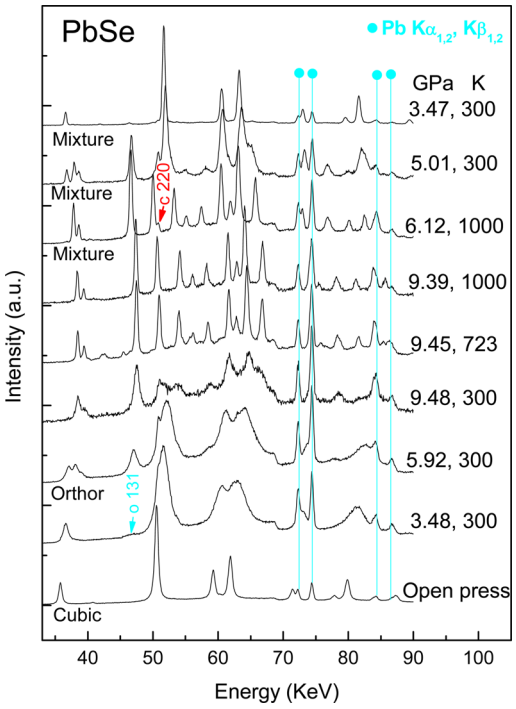

Figure 1. Selected energy-dispersive synchrotron XRD patterns of PbSe taken at different $P-T$ conditions. Cyan solid dots denote fluorescence K$\alpha_{1,2}$ and K$\beta_{1,2}$ peaks of Pb, which originate from PbSe and lead shielding of the detector. The red arrow marks the 220 peak of cubic PbSe observed at 6.12 GPa and 1000 K. The onset phase transition occurs at 3.48 GPa, and the cyan arrow denotes the 131 peak of orthorhombic phase.

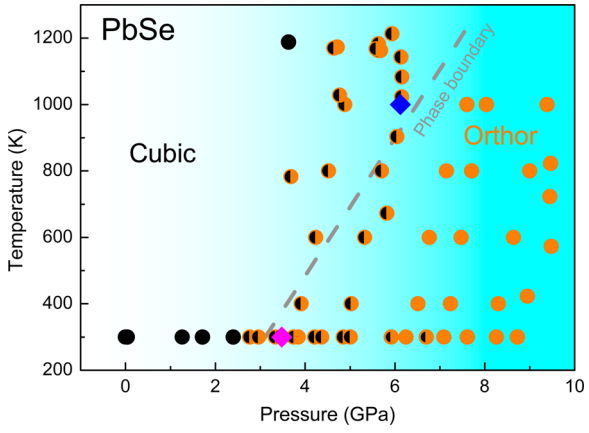

Figure 2. Phase diagram of PbSe determined using *in-situ* high-$P-T$ synchrotron XRD measurements. Black and orange solid dots represent the measured conditions for single-phase cubic- and orthorhombic-PbSe, respectively. The conditions for the co-existing phases are denoted by black−orange solid dots. During room temperature compression, the onset of the cubic → orthorhombic transition occurs at ∼3.48 GPa, denoted by a magenta diamond (see Figure 1). During decompression, the reverse orthorhombic-to-cubic phase transformation was first observed at ∼6.12 GPa and 1000 K (also see Figure 1), denoted as a blue diamond. On the basis of these observations, a tentative phase boundary between the cubic and orthorhombic PbSe is delineated as a gray dashed line.

of the high-P XRD data of PbSe are limited within the 45−85 keV range, and the observed peak intensities agree with the calculated values (see Supporting Information Figure S1). Thus, the crystal structure can properly be refined using such energy-dispersive XRD data. In fact, the suitability of energy-dispersive XRD data for structural refinements have been successfully demonstrated (refs 30 and 35). Moreover, for orthorhombic PbSe, the structural differences between *B*33 and *B*16 are mainly reflected by a number of extra, weak Bragg reflections in the latter. For a structureless Le Bail fitting, the analyses were carried out in a wider energy range 20−90 keV. Figure 3a shows the refined XRD pattern of cubic-PbSe taken

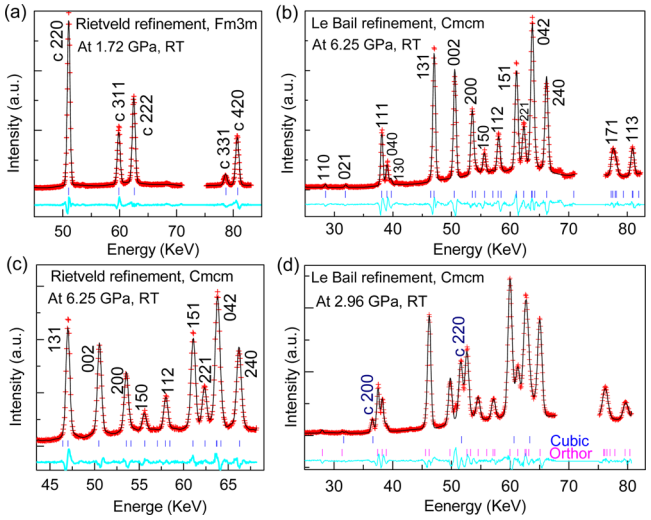

Figure 3. Refined synchrotron XRD patterns for cubic and orthorhombic PbSe collected on compression and quenched from high temperature. Red crosses and black lines represent the observed and calculated profiles, respectively. The difference curves between the observed and calculated profiles are shown in cyan. The blue and magenta tick marks correspond to the allowed peak positions of Bragg reflections for PbSe. (a) Rietveld analysis of cubic phase at 1.72 GPa. (b) Le Bail fit of orthorhombic PbSe at 6.25 GPa. (c) Rietveld refinement in an energy range 40−75 keV. (d) Le Bail analysis of co-existing cubic and orthorhombic phases at 2.96 GPa. The subtracted portions around 73 and 85 keV correspond to Pb fluorescence peaks.

at 1.72 GPa and room temperature. As shown in Figure 3b, all new diffraction peaks observed at 6.25 GPa can be indexed by an orthorhombic symmetry. Le Bail refinement is initially performed on the new phase by either *B*33 or *B*16, the two most frequently reported structural candidates.[21−23,36−38] The observed XRD pattern can be refined very well by either of them with high figure-of-merit values. Similar situations also occur in Rietveld structural refinements, as shown in Figure 3c. The details of the refined structural parameters are summarized in Table 1. At 2.96 GPa, both *B*1 and *B*33 phases co-exist in Figure 3d. As will be discussed below, the *Cmcm* *B*33-type structure is more favorable for orthorhombic PbSe.

The plot in Figure 4a shows the experimental XRD pattern collected at 4.85 GPa and room temperature during decompression. The PbSe sample is predominantly orthorhombic, although a very small fraction of cubic phase co-exists, as denoted by the *c220* peak at ∼51 keV. To clarify the structural controversy between *Cmcm* and *Pnma*, we simulated the theoretical XRD patterns using the obtained structural parameters in Table 1, and the corresponding structures are depicted in Figure 4b in polyhedral views. Remarkably, both of the computed patterns, including the peak intensity, agree well with the experimental observations in the energy region 40−70 keV. As a result, as shown in Figure 4b, the two structural

DOI: 10.1021/acs.inorgchem.5b00591
Inorg. Chem. 2015, 54, 4981−4989

Table 1. Summary of Structural Parameters for Orthorhombic PbSe Determined by Rietveld Analyses of Synchrotron XRD Data

	B33, *Cmcm*	*B16*, *Pnma*
P–*T* conditions	6.25 GPa, 300 K	6.25 GPa, 300 K
syst	orthorhombic	orthorhombic
Strukturbericht designation	*B33*	*B16*
space group	*Cmcm* (No. 63)	*Pnma* (No. 62)
formula	Pb_4Se_4	Pb_4Se_4
cell params (Å)	a = 4.0930(3), b = 11.2337(4), c = 4.3365(3)	a = 11.2337(4), b = 4.3365(3), c = 4.0930(3)
cell volume (Å^3)	199.390	199.390
density (g cm^{-3})	9.533	9.533
Pb Wyckoff site	4*c*, (0, 0.3765(5), $^1/_4$)[a]	4*c*, (0.1226(5), $^1/_4$, 0.4864(5))[a]
Se Wyckoff sites	4*c*, (0, 0.1369(5), $^1/_4$)[a]	4*c*, (0.3597(5), $^1/_4$, 0.4897(5))[a]
d_{Pb-Se} (Å)	2.6916, 2.9853, 3.5701	2.6634, 2.9789, 2.9973, 3.6162, 3.6498
wR_P (%), R_P (%), χ^2	5.6, 4.4, 4.0	5.8, 4.5, 4.1

[a]The atomic sites in *Cmcm* and *Pnma* are 4*c*, (*x*, *y*, *z*) (*x* = 0 and *z* = $^1/_4$) and 4*c*, (*x*′, *y*′, *z*′) (*y*′ = $^1/_4$), respectively, which satisfy the following operations: $x = z' - {}^1/_2$, $y = {}^1/_2 - x'$, and $z = y'$. On the basis of the obtained results, the main difference between the two structural modes lies in their z'_{Pb} and z'_{Se} values, both of which deviate from 1/2, giving rise to a number of additional weak Bragg reflections in *Pnma* (see Figure 4).

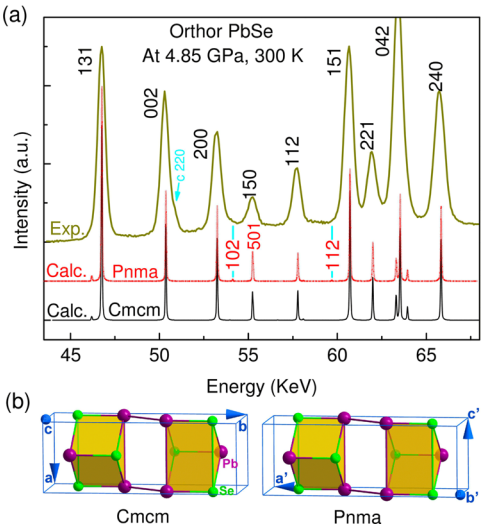

Figure 4. (a) Observed and calculated XRD patterns of orthorhombic PbSe at 4.85 GPa and 300 K. The calculated patterns are based on two structural models of *Cmcm* (No. 63) and *Pnma* (No. 62). The structural parameters of *Cmcm* used in the simulation are a = 4.1227(3) Å, b = 11.3412(4) Å, and c = 4.3626(3) Å, and the refined atomic positions are listed in Table 1. For *Pnma*, simulations are performed by using the lattice parameters of a = 11.3412(4) Å, b = 4.3626(3) Å, and c = 4.1227(3) Å. The refined atomic positions are Pb, 4*c* (x, $^1/_4$, z) (x = 0.1226(5) Å, z = 0.4864(5) Å), and Se, 4*c* (x, $^1/_4$, z) (x = 0.3597(5) Å, z = 0.4897(5) Å). (b) Crystal structures of *Cmcm* and *Pnma* in polyhedral views. For comparison, the atomic sites of *Pnma* phase are constrained by $z_{Pb} = z_{Se} = {}^1/_2$. It is noted that either z_{Pb} or z_{Se} deviating from $^1/_2$ will lead to new Bragg reflections (e.g., 102 and 112) without significantly modifying the main peak intensities.

models are essentially indistinguishable when the atomic coordinate z values for *Pnma* are fixed at $z_{Pb} = z_{Se} = {}^1/_2$.

For the cases of $z_{Pb} = z_{Se} < {}^1/_2$ in *Pnma*, an additional set of diffraction peaks, such as 102 and 112, appear in the calculated pattern (Figure 4a). The calculated intensities, however, diminish rapidly to zero when z_{Pb} and z_{Se} approach $^1/_2$, as shown in Figure 5a. The fact that no such diffraction peaks are

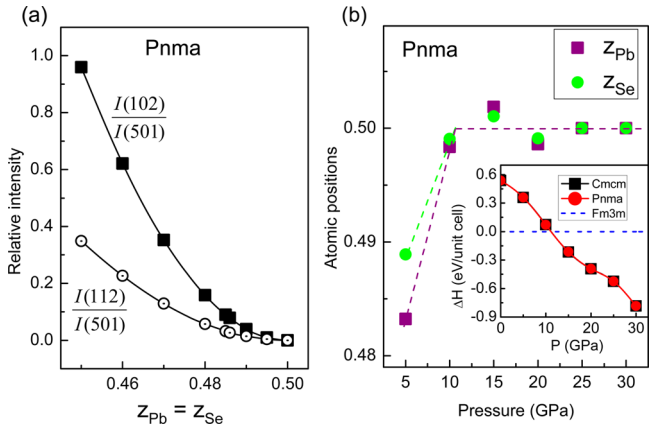

Figure 5. (a) Calculated peak intensity of 102 and 112 of *Pnma* normalized to that of 501 (see Figure 4a) as a function of coordinate values of z_{Pb} and z_{Se}. Both z_{Pb} and z_{Se} are fixed equivalently during the simulation. (b) First-principles calculations of atomic positions of z_{Pb} and z_{Se} as a function of pressure for *Pnma*-PbSe. Inset is the calculated pressure dependence of enthalpy differences (ΔH) between orthorhombic and cubic PbSe.

observed in the experimental patterns (see Figures 3 and 4) suggests $z_{Pb} \approx z_{Se} = {}^1/_2$, although the refined values are z_{Pb} = 0.4864(5) and z_{Se} = 0.4897(5) (see Table 1) for the *Pnma* phase. Such deviations are mainly attributed to additional weak peaks (e.g., 102 and 112 in Figure 4a) due to the background contributions. For the refined z-position tolerance value (i.e., ±0.0005), it is solely given by the GSAS program and cannot arbitrarily be overused for the current case. Under such circumstances (i.e., $z_{Pb} = z_{Se} = {}^1/_2$), *Pnma* is virtually structurally equivalent to *Cmcm*, because the atomic sites in *Cmcm* (i.e., 4*c* (0, y_{cmcm}, $^1/_4$)) and *Pnma* (i.e., 4*c* (x_{pnma}, $^1/_4$, z_{pnma})) satisfy the following operations:

$$x_{cmcm} = z_{pnma} - \frac{1}{2}$$

$$y_{cmcm} = \frac{1}{2} - x_{pnma}$$

$$z_{cmcm} = y_{pnma}$$

Therefore, the higher-symmetry *Cmcm* is a more appropriate structure for orthorhombic PbSe than its parent space group *Pnma*, because, as a general rule, the higher symmetric space group is often used for determination of crystal structure. Using first-principles calculations, as shown in Figure 5b, the optimized z_{Pb} and z_{Se} of *Pnma* are close to $^1/_2$ as pressure approaches the theoretical transition pressure of the *B*1 → orthorhombic at ∼11 GPa (see inset of Figure 5b), which supports our experimental results. As expected, from their equivalence in symmetry, both *Cmcm* and *Pnma* exhibit almost the same enthalpy at high pressures, which is consistent with the previous report.[17] Therefore, we conclude that orthorhombic PbSe adopts a *Cmcm* structure, a higher symmetry

DOI: 10.1021/acs.inorgchem.5b00591
Inorg. Chem. 2015, 54, 4981−4989

than *Pnma*, which is isotypic with the structure of indium iodide (InI) or thallium iodide (TlI).[39]

For *Cmcm*-type lead chalcogenides, there is still some debate, from both experimental[20,40] and theoretical studies,[14,26] between InI-type and *anti*-InI-type structural models. Using these two models, we simulated XRD patterns of *Cmcm* PbSe, as shown in Figure 6a. Also plotted is a pattern observed at 6.25 GPa. Evidently, *anti*-InI-type "SePb" is an incorrect structure, because some observed reflections are absent (e.g., peak 150) while a subset of new diffraction peaks emerges in "SePb". In contrast, the simulated XRD pattern based on the InI-type structure agrees very well with our observations. Moreover, the refined atomic positions, 4*c*(0, *y*, $^1/_4$), of *Cmcm*-PbSe are y_{Pb} = 0.3765(5) and y_{Se} = 0.1369(5) (see Table 1), which are consistent with the first-principles calculations as shown in Figure 6b. These calculations also show that the Pb and Se atoms continuously displace along the *y*-axis with increasing pressure, indicating that *Cmcm* is an energetically unstable phase at higher pressures. Such atomic motions, as reported in previous studies,[10,24] would eventually lead to the *Cmcm* → *Pm3m* phase transition. In short, the success in structural resolution of orthorhombic PbSe in this work will open a new avenue for the study of the high-*P* intermediate phases of heavy-metal chalcogenides including II–VI (e.g., HgTe)[41−43] and IV–VI (e.g., PbTe) semiconductors.[25] Previous studies on this class of compounds failed to resolve their intermediate high-*P* intermediate structures, largely because high-*P* measurements were conducted at room temperature only (vs high temperature), where the XRD patterns exhibit severe peak broadening and overlap.

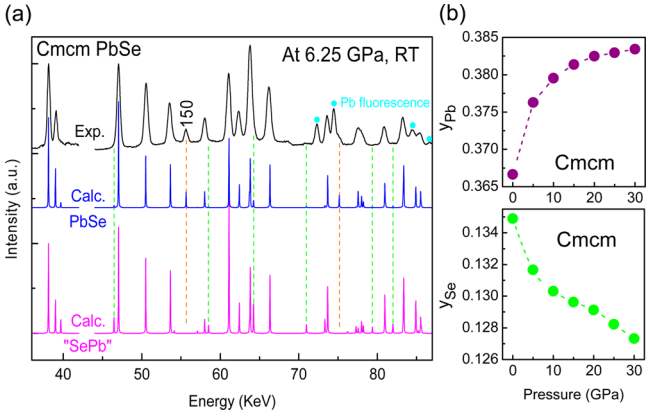

Figure 6. (a) Observed and calculated XRD patterns at 6.25 GPa and 300 K. InI-type PbSe and *anti*-InI–type "SePb" were used for the calculations; the only difference between them is the atomic positions. The detailed structural parameters for InI-type PbSe are listed in Table 1. For "SePb", the atomic positions of 4*c* (0, *y*, $^1/_4$) are *y* = 0.3765(5) and 0.1369(5) for Se and Pb, respectively. The XRD patterns are normalized for the energy regions of 35–42 and 44–87 keV, respectively. (b) Calculated atomic sites of y_{Pb} and y_{Se} of *Cmcm*-PbSe as a function of pressure, obtained from first-principles simulations.

Figure 7 summarizes the measured pressure–volume (*P*–*V*) data of PbSe at selected temperatures of 300, 400, 600, 800, and 1000 K. Bulk modulus, K_0, values of both cubic and orthorhombic phases are derived from the fit of these data to a second-order Birch–Murnaghan equation of state.[44] Because of the limited pressure range of the present study that inhibits an accurate constraint on pressure derivative of bulk modulus

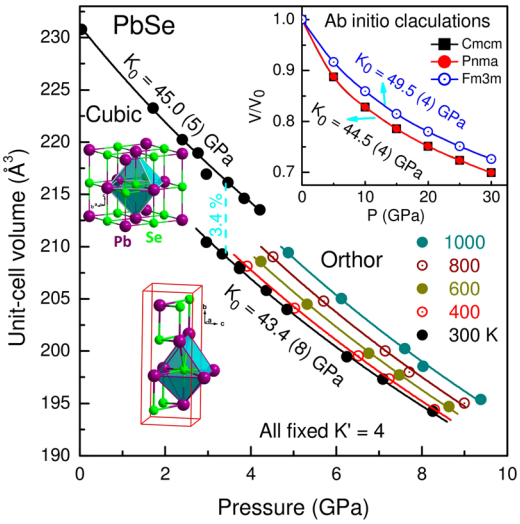

Figure 7. Isothermal volume–pressure data of orthorhombic phase collected at 300, 400, 600, 800, and 1000 K, respectively. The volume–pressure data of cubic phase was also collected at 300 K. All data are fitted to the second-order Birch–Murnaghan equation of state. Insets are the corresponding crystal structures depicted in polyhedral views. Also shown in the upper right corner are the calculated *P*–*V* data of *Cmcm* and *Pnma* PbSe.

($K' = \partial K_0/\partial P$), we fixed K' at 4. The detailed analysis of the isothermal *P*–*V* data has been described in ref 30. At 300 K, the cubic–orthorhombic transition is accompanied by a ~3.4% volume reduction, close to the ~3.8% reduction reported for PbS, indicating that orthorhombic-PbSe is a high-*P* phase with a higher density. The derived ambient bulk moduli of cubic- and orthorhombic-PbSe are K_0 = 45.0 (5) and 43.4 (8) GPa, respectively. Interestingly, the high-density orthorhombic phase is slightly more compressible than low-*P* cubic-PbSe. Such anomalous elastic softening has also been found in its sister material PbS, which shows a substantially larger reduction, ~50%, at the cubic–orthorhombic transition.[9] This phenomenon is against the common physical intuition and has only rarely been reported in other compound systems. To confirm such a behavior, *ab initio* simulations were carried out on PbSe (see the Experimental and Calculation Methods for details). As shown in the inset of Figure 7, the computed bulk moduli for *Fm3m* and *Cmcm* phases are 49.5 (4) and 44.5 (4) GPa, respectively, when K' is fixed at 4, in excellent agreement with the experimental values. By using a third-order Birch–Murnaghan equation of state,[44] we obtained K_0 = 47.6(3) GPa/K' = 4.2 and K_0 = 33.4(3) GPa/K' = 5.2, respectively, for the *Fm3m* and *Cmcm* phases, which agree well with previous theoretical calculations.[17,45] Clearly, for both fitting schemes the calculations support the experimental finding of phase-transition induced elastic softening in PbSe. For comparison, we also computed the *P*–*V* data of *Pnma*-PbSe (inset of Figure 7), which are essentially identical to those of *Cmcm* phase.

To shed light on mechanisms underlying the phase-transition induced elastic softening, we refined the structures of cubic- and orthorhombic-PbSe using a XRD pattern with both phases co-existing at 2.96 GPa and 300 K (see Figure 3d). The detailed structural parameters are summarized in Table 2. Strikingly, two of the three Pb–Se bonds in the high-density orthorhombic phase are extended relative to the low-*P* cubic phase (see Table 2), which agrees well with the coordination–distance paradox, in the sense that the cation–anion bond

DOI: 10.1021/acs.inorgchem.5b00591
Inorg. Chem. 2015, 54, 4981–4989

Table 2. Summary of Structural Parameters for PbSe Phases Determined by Le Bail Analyses of XRD Data

	cubic, *Fm*3*m*	orthorhombic, *Cmcm*
P−*T* conditions	2.96 GPa, 300 K	2.96 GPa, 300 K
structure	NaCl-type	InI-type
Strukturbericht designation	*B*1	*B*33
formula	Pb_4Se_4	Pb_4Se_4
cell params (Å)	a = 6.0072(8)	a = 4.1638(6), b = 11.4688(8), c = 4.4062(6)
cell volume (Å^3)	216.779	210.413
density (g cm^{-3})	8.492	9.533
d_{Pb-Se} (Å)	3.0036	2.6906, 3.0371, 3.6877
d_{Pb-Pb} (Å)	4.2477	3.6053, 4.1638, 4.1815, 4.4062
wR_P (%), R_P (%), χ^2	8.3, 5.6, 5.5	

length of the high-*P* phase often increases as the coordination increases.[46] For PbSe, the Pb atoms in the *Cmcm* phase are 7-fold coordinated with the Se atoms, whereas they are 6-fold coordinated in the cubic phase (see Figure 7). On the other hand, three of the four Pb−Pb bonds become shortened in the *Cmcm* phase; the shortest bond is 3.6053 Å, close to the interatomic distance in lead metal (~3.5 Å). In addition, plotted in Figure 8a is the variation of lattice parameters as a

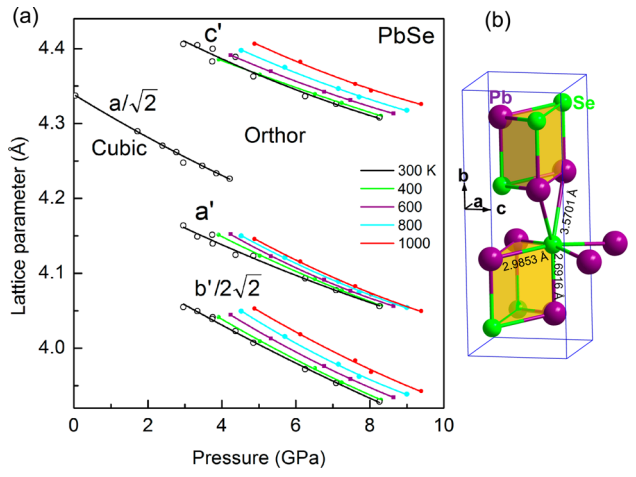

Figure 8. (a) Isothermal lattice parameters of orthorhombic PbSe as a function of pressure collected at 300, 400, 600, 800, and 1000 K. The 300 K data were also collected for cubic phase. (b) A polyhedral view of *Cmcm*-PbSe. The refined Pb−Se bond lengths are 2.6916, 2.9853, and 3.5701 Å at 6.25 GPa and 300 K (see Table 1).

function of pressure at several selected temperatures (also see Table 5). At 300 K, the *b*′-axis, the longest lattice parameter in orthorhombic-PbSe, is more compressible than the *a*′- and *c*′-axes. The compressibility of both *a*′- and *c*′-axes is close to that of the *a*-axis in the cubic phase, as the corresponding lattices show a similar trend at high pressures. From this point of view, the reduced incompressibility of the *b*′-axis should be responsible for elastic softening in PbSe. In fact, both cubic and orthorhombic phases are structurally composed of trigonal prisms (see Figure 8b); the transition between them mainly involves the translation of trigonal prisms (ref 9). However, the trigonal prisms in *Cmcm*-PbSe are loosely stacked along the *b*′-axis (Figure 8b), because the Pb−Se bond is significantly prolonged, indicating the characteristic of a weak bonding along this axis. We thus conclude that the pressure-induced elastic softening in PbSe is presumably attributed to such changes in bonding at high pressures, especially the loosely bonded trigonal prisms along the *b*′-axis in the orthorhombic structure.

By fitting of the isothermal *P*−*V* data sets in Table 3 and Figure 7, the high-temperature bulk modulus (K_T) and zero-pressure volume (V_T) are derived, which are shown in parts a and b of Figure 9, respectively. The obtained data are listed in Table 4. Linear regression of the K_T data in Figure 9a of orthorhombic-PbSe with the equation

$$K_T = K_0 + \left(\frac{\partial K_T}{\partial T}\right)_P (T - 300) \quad (1)$$

yields $(\partial K_T/\partial T)_P = -8.0(9) \times 10^{-3}$ GPa K^{-1} and K_0 = 43.2(5) GPa. As shown in Figure 9b, thermal expansivity at zero pressure is calculated for orthorhombic-PbSe using the zero-pressure V_T data and the equation

$$V_T = V_0 \exp\left(\int_{300K}^{T} \alpha_T \, dT\right) \quad (2)$$

where α_T is expressed as

$$\alpha_T = \alpha_0 + \alpha_1 T \quad (3)$$

The least-squares fit yields $\alpha_0 = 5.2\ (9) \times 10^{-5}$ K^{-1} and $\alpha_1 = 1.4\ (1) \times 10^{-9}$ K^{-2}.

A more general *P*−*V*−*T* equation can be expressed as $P(V, T) = P_0(V) + P_{th}$, where $P_0(V)$ (i.e., P_{calc} in Table 3) can be given by the Birch−Murnaghan equation of state and P_{th} is thermal pressure. This thermal pressure approach is also useful for deriving $(\partial K_T/\partial T)_V$, the temperature derivative of bulk modulus at constant volume, which is experimentally difficult to measure. P_{th} is the difference between the observed pressure at a given temperature and the calculated pressure from the Birch−Murnaghan equation of state at 300 K with both pressures corresponding to the same volume. The thus-obtained thermal pressures for orthorhombic-PbSe are shown in Figure 9c and Table 3, which reveal that thermal pressures vary linearly with temperature, a trend that has also been found in many other phases.[47] P_{th} at any temperature above 300 K can also be expressed by Anderson's thermodynamic equation

$$P_{th} = \left[\alpha K_T(V_0, T) + \left(\frac{\partial K_T}{\partial T}\right)_V \ln\left(\frac{V_0}{V}\right)\right](T - 300) \quad (4)$$

Using this equation, from the least-squares fit of the P_{th}−*T* data in Figure 9c and the measured volume data in Table 3, the obtained values of $\alpha K_T(V_0, T)$ and $(\partial K_T/\partial T)_V$ are 1.9 (3) × 10^{-3} and −2.0 (30) × 10^{-3} GPa K^{-1}, respectively. It is worth mentioning that the $(\partial K_T/\partial T)_V$ is very small, suggesting that the P_{th} is nearly independent of unit cell volume or pressure. Indeed, the P_{th} versus pressure data plotted in Figure 9d along all isotherms can be approximately fitted by constant values of thermal pressure. On the basis of the thermodynamic identity

$$\left(\frac{\partial K_T}{\partial T}\right)_V = \left(\frac{\partial K_T}{\partial T}\right)_P + \left(\frac{\partial K_T}{\partial P}\right)_T \alpha K_T(V_0, T) \quad (5)$$

the calculated $(\partial K_T/\partial T)_P$ value is -7.6×10^{-3} GPa K^{-1} at fixed $K' = (\partial K_T/\partial P)_T = 4$, which is in excellent agreement with the value derived in Figure 9a.

To investigate the electrical properties of PbSe, *in-situ* high-*P* electrical resistance measurement was performed on a single-crystal sample at room temperature (see Experimental and Calculation Methods for details). Cubic lead chalcogenides

DOI: 10.1021/acs.inorgchem.5b00591
Inorg. Chem. 2015, 54, 4981−4989

Table 3. Obtained Pressure−Volume Data of Orthorhombic PbSe at 300, 400, 600, 800, and 1000 K.[a]

T (K)	P (GPa)	V (Å^3)	P_{calc}[b] (GPa)	P_{th}[b] (GPa)	T (K)	P (GPa)	V (Å^3)	P_{calc} (GPa)	P_{th} (GPa)
300	8.26	194.1691	8.23	0.04	600	8.64	194.6846	8.03	0.62
300	7.09	197.2292	7.10	−0.01	600	7.48	197.7002	6.93	0.55
300	6.25	199.3901	6.35	−0.10	600	6.77	199.7813	6.22	0.55
300	4.85	203.8980	4.90	−0.05	600	5.33	204.4675	4.73	0.60
300	4.37	205.9704	4.29	0.09	600	4.24	208.5707	3.55	0.69
300	3.75	208.1759	3.66	0.10	800	9.00	195.0089	7.91	1.10
300	3.74	207.8571	3.75	−0.01	800	7.71	197.9769	6.84	0.88
300	3.34	209.3010	3.35	−0.02	800	7.15	200.0136	6.14	1.02
300	2.96	210.4136	3.06	−0.10	800	5.71	204.7692	4.64	1.07
400	8.31	194.3945	8.14	0.17	800	4.53	209.0144	3.43	1.10
400	7.24	197.3340	7.06	0.18	1000	9.39	195.3599	7.78	1.61
400	6.52	199.5443	6.30	0.23	1000	8.04	198.5264	6.65	1.40
400	5.03	204.1057	4.84	0.20	1000	7.61	200.2415	6.07	1.55
400	3.92	208.1307	3.67	0.25	1000	6.12	205.0170	4.57	1.56
					1000	4.89	209.4131	3.32	1.57

[a] P, P_{calc}, and P_{th} represent the measured, calculated, and thermally induced pressures, respectively. [b] P_{calc} and P_{th} can be expressed using $P_{calc} = {}^3/_2 K_0[(V_0/V)^{(7/3)} - (V_0/V)^{(5/3)}]$ and $P_{th} = P - P_{calc}$, where P is the measured pressure at a given high-temperature and P_{calc} is the calculated pressure at 300 K, both of which refer to the same volume. The ambient bulk modulus, K_0, and unit-cell volume, V_0, are 43.4 (8) GPa and 223.9 (2) Å^3, respectively, which were derived from the 300 K isothermal equation of state.

Table 4. High-T Bulk Moduli and Zero-Pressure Volumes of Orthorhombic PbSe Obtained from the Fits of Isothermal Data Sets to the Second-Order Birch−Murnaghan Equation of State[a]

	orthorhombic PbSe				
T (K)	300	400	600	800	1000
K_T (GPa)	43.4(8)	41.7(10)	40.0(10)	38.6(10)	37.6(10)
V_T (Å^3)	223.9(2)	225.4(1)	227.5(3)	230.0(3)	232.5(3)

[a] See Figure 7.

Table 5. Measured Lattice Parameters of Cubic and Orthorhombic PbSe under High-Pressure and High-Temperature Conditions

T (K)	P (GPa)	a (Å)	b (Å)	c (Å)	T (K)	P (GPa)	a (Å)	b (Å)	c (Å)
				Orthorhombic					
300	8.26	4.0566	11.1217	4.3052	600	8.64	4.056	11.128	4.3133
300	7.09	4.0776	11.1889	4.3250	600	7.48	4.0765	11.1971	4.3313
300	6.25	4.0921	11.2401	4.3367	600	6.77	4.0913	11.2458	4.3422
300	4.85	4.1227	11.3412	4.3626	600	5.33	4.1225	11.3498	4.3699
300	4.37	4.1233	11.3860	4.3838	600	4.24	4.1522	11.4392	4.3911
300	3.75	4.1384	11.4416	4.3948	800	9.00	4.0542	11.1404	4.3177
300	3.74	4.1502	11.4305	4.3824	800	7.71	4.0746	11.2069	4.3355
300	3.34	4.1472	11.4657	4.4013	800	7.15	4.0892	11.2528	4.3467
300	2.96	4.1638	11.4688	4.4062	800	5.71	4.1208	11.3579	4.3750
400	8.31	4.0565	11.1185	4.3101	800	4.53	4.1499	11.4530	4.3976
400	7.24	4.0772	11.1842	4.3274	1000	9.39	4.0496	11.1513	4.3261
400	6.52	4.0922	11.2375	4.3392	1000	8.04	4.0717	11.2236	4.3442
400	5.03	4.1234	11.3393	4.3653	1000	7.61	4.0829	11.2670	4.3529
400	3.92	4.1515	11.4312	4.3857	1000	6.12	4.1157	11.3663	4.3826
					1000	4.89	4.1457	11.4628	4.4067
				Cubic					
300	4.21	5.9769			300	2.77	6.0273		
300	3.85	5.9871			300	2.40	6.0389		
300	3.47	6.0012			300	1.72	6.0664		
300	2.96	6.0072			300	0.00	6.1339		

PbX (X = S, Se, and Te) are a class of highly degenerate semiconductors,[48] indicating that most carriers are not thermally activated over the band gap. Indeed, these compounds exhibit positive temperature dependence of band gap,[12,49] which is contrary to that of conventional semiconductors (e.g., hexagonal GaN).[13] Therefore, the electrical resistivity of PbX is mainly attributed to carrier concentration and carrier mobility and only weakly correlates with the band gap. Figure 10 shows the measured electrical resistance of PbSe against pressure, $R(P)$. A clear resistivity jump corresponds to

DOI: 10.1021/acs.inorgchem.5b00591
Inorg. Chem. 2015, 54, 4981−4989

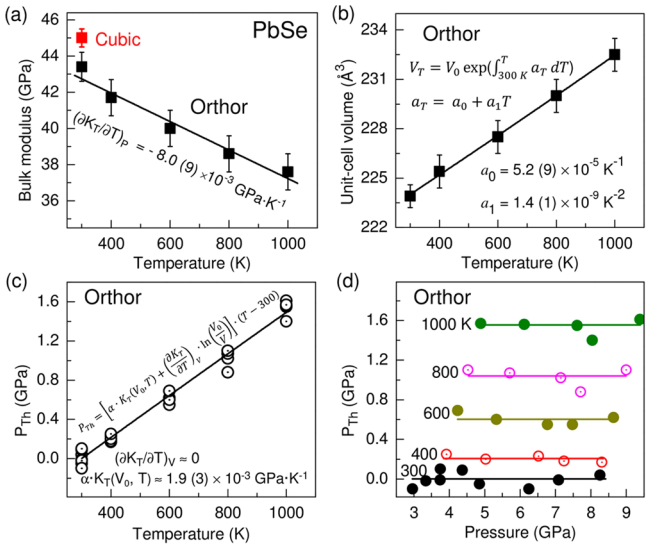

Figure 9. Thermoelastic properties of orthorhombic PbSe derived from the measured $P-V-T$ data. (a) Bulk modulus of orthorhombic phase as a function of temperature. The bulk modulus of cubic phase at 300 K is also plotted for comparison. (b) Volumetric thermal expansion at atmospheric pressure. (c) Thermal pressure, P_{th}, as a function of temperature. (d) P_{th} as a function of pressure.

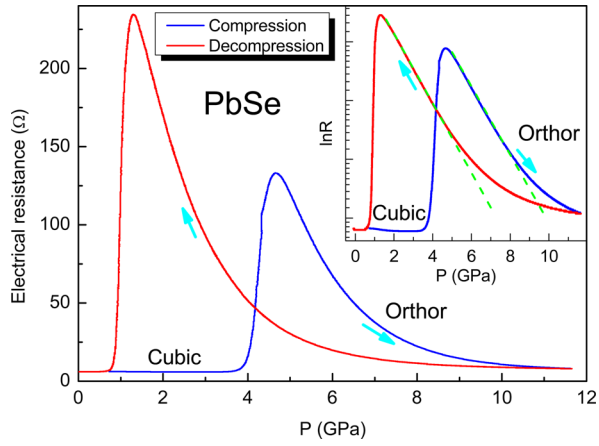

Figure 10. Electrical resistance of PbSe as a function of pressure at room temperature. The measurements were performed upon compression and decompression as denoted by cyan arrows. Inset shows the resistance data in a logarithm scale, ln R, against pressure. Dashed green lines are the linear fits of ln R vs pressure. Because the experimental pressure was precalibrated by an *ex-situ* method performed on compression at room temperature, it is slightly different from that of the *in-situ* XRD measurement (see Figure 1).

the cubic–orthorhombic structural transition during compression, likely because the scattering parameters of carriers and other related parameters are significantly enhanced at the phase transition, which would eventually lower the carrier mobility. The measured onset pressure for the phase transition is ~3.7 GPa, which is close to the value of 3.48 GPa obtained in our high-P synchrotron experiment (see Figure 1). The phase transition appears to complete at ~4.8 GPa, when the resistance approaches a maximum value that is ~22 times that of the cubic phase. Upon further compression, the $R(P)$ deceases exponentially with pressure up to ~8 GPa (see inset in Figure 10), followed by a complicated transport behavior as the slope of dR/dP rapidly approaches zero. Above ~11 GPa, the resistance is saturated at ~8 Ω, which is only slightly higher than that of the cubic phase (~6 Ω). Although a previous report on PbSe shows a large pressure dependence of the band gap,[50] the measured electrical resistance for cubic PbSe levels off at a constant value of ~6 Ω (see Figure 10), further suggesting a weak correlation between electrical resistivity and band gap in PbSe. Therefore, all these electrical transport behaviors are primarily associated with carrier concentration and carrier mobility in PbSe, which vary with pressure. However, several recent studies show a large negative pressure dependence of resistance in cubic-PbSe at low pressures, which may be attributed to the loosely packed powder samples used in their experiments.[2,24,51] Different from the case of single-crystal sample in our experiment, the electrical connection between crystals of the loosely packed powders is often poor and shows a strong pressure dependence of conductivity at low pressure.

During decompression, the $R(P)$ behaves similarly to that during compression (see Figure 10). The observed phase-transition pressure is ~1.4 GPa, which, as expected from the kinetics of the solid-state phase transformation, is much lower than that measured during compression (~3.7 GPa) (see Figure 2). Besides, the observed peak resistance value is nearly twice that obtained during compression, presumably because carrier mobility becomes further lowered in the orthorhombic phase at a much lower pressure of ~1.4 GPa.

CONCLUSIONS

In summary, the pressure-induced phase transition in PbSe was investigated by using *in-situ* high-energy-dispersive synchrotron X-ray diffraction, high-P resistance measurement, and *ab initio* calculations. For the first time, the high-quality X-ray diffraction patterns of the orthorhombic intermediate phase of PbSe were collected under high $P-T$ conditions. On the basis of these data, structural refinements clearly show that orthorhombic PbSe adopts an InI-type, $B33$ structure with the *Cmcm* (No. 63) space group. At room temperature, the cubic-to-orthorhombic phase transition starts at ~3.48 GPa on compression with ~3.4% volume reduction, and both phases co-exist in a wide high-$P-T$ range. Moreover, a number of thermoelastic parameters of orthorhombic PbSe are deduced on the basis of the $P-V-T$ measurements.

ASSOCIATED CONTENT

Supporting Information

Observed and calculated energy-dispersive XRD patterns for cubic- and orthorhombic-PbSe. The Supporting Information is available free of charge on the ACS Publications website at DOI: 10.1021/acs.inorgchem.5b00591.

AUTHOR INFORMATION

Corresponding Authors

*E-mail: ShanminWang@gmail.com.
*E-mail: Yusheng.Zhao@UNLV.edu.

Notes

The authors declare no competing financial interest.

ACKNOWLEDGMENTS

This work is partially supported by UNLV High Pressure Science and Engineering Center (HiPSEC), which is a DOE NNSA Center of Excellence operated under Cooperative Agreement DE–FC52–06NA27684, and UNLV start–up

DOI: 10.1021/acs.inorgchem.5b00591
Inorg. Chem. 2015, 54, 4981–4989

funding to Y. Zhao. This work was also supported by the China 973 Program (Grant No. 2011CB808205), and the National Natural Science Foundation of China (Grant Nos. 11427810 & 51472171). Los Alamos National Laboratory is operated by Los Alamos National Security LLC, under DOE Contract DE-AC52-06NA25396. Use of the National Synchrotron Light Source (at X17B2 beamline), Brookhaven National Laboratory, was supported by DOE−BES, under Contract No. DE−AC02−98CH10886.

REFERENCES

(1) Pei, Y. Z.; LaLonde, A.; Iwanaga, S.; Snyder, G. J. *Energy Environ. Sci.* **2011**, *4*, 2085−2089.
(2) Ovsyannikov, S. V.; Shchennikov, V. V.; Popova, S. V.; Derevskov, A. Y. *Phys. Status Solidi B* **2003**, *235*, 521−525.
(3) Korkosz, R. J.; Chasapis, T. C.; Lo, S.-h.; Doak, J. W.; Kim, Y. J.; Wu, C.-I.; Hatzikraniotis, E.; Hogan, T. P.; Seidman, D. N.; Wolverton, C.; Dravid, V. P.; Kanatzidis, M. G. *J. Am. Chem. Soc.* **2014**, *136*, 3225−3237.
(4) Lee, S.; Esfarjani, K.; Luo, T.; Zhou, J.; Tian, Z.; Chen, G. *Nat. Commun.* **2014**, *5*, 3525.
(5) Bozin, E. S.; Malliakas, C. D.; Souvatzis, P.; Proffen, T.; Spaldin, N. A.; Kanatzidis, M. G.; Billinge, S. J. L. *Science* **2010**, *330*, 1660−1663.
(6) Jensen, K. M. Ø.; Božin, E. S.; Malliakas, C. D.; Stone, M. B.; Lumsden, M. D.; Kanatzidis, M. G.; Shapiro, S. M.; Billinge, S. J. L. *Phys. Rev. B* **2012**, *86*, 085313.
(7) Delaire, O.; Ma, J.; Marty, K.; May, A. F.; McGuire, M. A.; Du, M. H.; Singh, D. J.; Podlesnyak, A.; Ehlers, G.; Lumsden, M. D.; Sales, B. C. *Nat. Mater.* **2011**, *10*, 614−619.
(8) Zhang, Y.; Ke, X.; Kent, P. R. C.; Yang, J.; Chen, C. *Phys. Rev. Lett.* **2011**, *107*, 175503.
(9) Wang, S.; Zhang, J.; Zhang, Y.; Alvarado, A.; Attapattu, J.; He, D.; Wang, L.; Chen, C.; Zhao, Y. *Inorg. Chem.* **2013**, *52*, 8638−8643.
(10) Chattopadhyay, T.; Werner, A.; von Schnering, H. G.; Pannetier, J. *Rev. Phys. Appl.* **1984**, *19*, 807−813.
(11) Wei, S.-H.; Zunger, A. *Phys. Rev. B* **1997**, *55*, 13605−13610.
(12) Lead selenide (PbSe) energy gap and band structure. In *Non-Tetrahedrally Bonded Elements and Binary Compounds I*; Madelung, O., Rössler, U., Schulz, M., Eds.; Springer: Berlin, 1998; Vol. *41C*.
(13) Gallium nitride (GaN), enery gap, exciton binding energy. In *Group IV Elements, IV-IV and III-V Compounds. Part b—Electronic, Transport, Optical and Other Properties*; Madelung, O., Rössler, U., Schulz, M., Eds.; Springer: Berlin, 2002; Vol. *41A1b*, pp 1−20.
(14) Zagorac, D.; Doll, K.; Schön, J. C.; Jansen, M. *Phys. Rev. B* **2011**, *84*, 045206.
(15) Wheeler, K. T.; Walker, D.; Johnson, M. C. *Am. J. Sci.* **2007**, *307*, 590−611.
(16) Jiang, J. Z.; Gerward, L.; Secco, R.; Frost, D.; Olsen, J. S.; Truckenbrodt, J. *J. Appl. Phys.* **2000**, *87*, 2658−2660.
(17) Ahuja, R. *Phys. Status Solidi B* **2003**, *235*, 341−347.
(18) Lach-hab, M.; Keegan, M.; Papaconstantopoulos, D. A.; Mehl, M. J. *J. Phys. Chem. Solids* **2000**, *61*, 1639−1645.
(19) Nabi, Z.; Abbar, B.; Méçabih, S.; Khalfi, A.; Amrane, N. *Comput. Mater. Sci.* **2000**, *18*, 127−131.
(20) Streltsov, S. V.; Manakov, A. Y.; Vokhmyanin, A. P.; Ovsyannikov, S. V.; Shchennikov, V. V. *J. Phys.: Condens. Matter* **2009**, *21*, 385501.
(21) Knorr, K.; Ehm, L.; Hytha, M.; Winkler, B.; Depmeier, W. *Eur. Phys. J. B* **2003**, *31*, 297−303.
(22) Fan, D.; Zhou, W.; Wei, S.; Liu, J.; Li, Y.; Jiang, S.; Xie, H. *Chin. Phys. Lett.* **2010**, *27*, 086401.
(23) Chattopadhyay, T.; Vonschnering, H. G.; Grosshans, W. A.; Holzapfel, W. B. *Physica B+C* **1986**, *139*, 356−360.
(24) Ovsyannikov, S. V.; Shchennikov, V. V.; Manakov, A. Y.; Likhacheva, A. Y.; Ponosov, Y. S.; Mogilenskikh, V. E.; Vokhmyanin, A. P.; Ancharov, A. I.; Skipetrov, E. P. *Phys. Status Solidi B* **2009**, *246*, 615−621.
(25) Rousse, G.; Klotz, S.; Saitta, A. M.; Rodriguez-Carvajal, J.; McMahon, M. I.; Couzinet, B.; Mezouar, M. *Phys. Rev. B* **2005**, *71*, 224116.
(26) Ferhat, D.; Savas, B. *Phys. Scr.* **2013**, *88*, 015603.
(27) Chen, J.; Yu, T.; Huang, S.; Girard, J.; Liu, X. *Phys. Earth Planet. Inter.* **2014**, *228*, 294−299.
(28) Weidner, D. J.; Vaughan, M. T.; Ko, J.; Wang, Y.; Liu, X.; Yeganeh-Haeri, A.; Pacalo, R. E.; Zhao, Y., Characterization of Stress, Pressure, and Temperature in SAm85, a Dia Type High Pressure Apparatus. In *High-Pressure Research: Application to Earth and Planetary Sciences*; American Geophysical Union: Terra Scientific Publishing Company (TERRAPUB): Tokyo, 2013; pp 13−17.
(29) Decker, D. L. *J. Appl. Phys.* **1971**, *42*, 3239−3244.
(30) Zhao, Y.; Von Dreele, R. B.; Weidner, D. J.; Schiferl, D. *High Pressure Res.* **1997**, *15*, 369−386.
(31) Toby, B. H. *J. Appl. Crystallogr.* **2001**, *34*, 210−213.
(32) Wang, W.; He, D.-W.; Wang, H.-K.; Wang, F.-L.; Dong, H.; Chen, H.; Li, Z.; Jian, Z.; Wang, S.; Kou, Z.; Peng, F. *Acta Phys. Sin.* **2010**, *59*, 3107−3115.
(33) Perdew, J. P.; Burke, K.; Ernzerhof, M. *Phys. Rev. Lett.* **1996**, *77*, 3865−3868.
(34) Kresse, G.; Joubert, D. *Phys. Rev. B* **1999**, *59*, 1758−1775.
(35) Zhao, Y.; Von Dreele, R. B.; Shankland, T. J.; Weidner, D. J.; Zhang, J.; Wang, Y.; Gasparik, T. *Geophys. Res. Lett.* **1997**, *24*, 5−8.
(36) Mariano, A. N.; Chopra, K. L. *Appl. Phys. Lett.* **1967**, *10*, 282−284.
(37) Chattopadhyay, T.; Pannetier, J.; Vonschnering, H. G. *J. Phys. Chem. Solids* **1986**, *47*, 879−885.
(38) Bencherif, Y.; Boukra, A.; Zaoui, A.; Ferhat, M. *Mater. Chem. Phys.* **2011**, *126*, 707−710.
(39) Jones, R. E.; Templeton, D. H. *Acta Crystallogr.* **1955**, *8*, 847.
(40) Grzechnik, A.; Friese, K. *J. Phys.: Condens. Matter* **2010**, *22*, 095402.
(41) Hu, J. Z. *Solid State Commun.* **1987**, *63*, 471−474.
(42) Nelmes, R. J.; McMahon, M. I.; Wright, N. G.; Allan, D. R. *Phys. Rev. B* **1995**, *51*, 15723−15731.
(43) McMahon, M. I.; Wright, N. G.; Allan, D. R.; Nelmes, R. J. *Phys. Rev. B* **1996**, *53*, 2163−2166.
(44) Birch, F. *Phys. Rev.* **1947**, *71*, 809−824.
(45) Skelton, J. M.; Parker, S. C.; Togo, A.; Tanaka, I.; Walsh, A. *Phys. Rev. B* **2014**, *89*, 205203.
(46) Neuhaus, A. *Chimia* **1964**, *18*, 93−103.
(47) Anderson, D. L. *Equations of State for Solids in Geophysics and Ceramic Science*; Oxford University Press: New York, 1994.
(48) Askerov, B. M. *Electron Transport Phenomena in Semiconductors*; World Scientific: Singapore, 1994.
(49) Gibbs, Z. M.; Kim, H.; Wang, H.; White, R. L.; Drymiotis, F.; Kaviany, M.; Jeffrey Snyder, G. *Appl. Phys. Lett.* **2013**, *103*, 262109.
(50) Zhuravlev, K. K.; Pietryga, J. M.; Sander, R. K.; Schaller, R. D. *Appl. Phys. Lett.* **2007**, *90*, 043110.
(51) Ovsyannikov, S. V.; Shchennikov, V. V.; Kar'kin, A. E.; Goshchitskii, B. N. *J. Phys.: Condens. Matter* **2005**, *17*, S3179.

DOI: 10.1021/acs.inorgchem.5b00591
Inorg. Chem. 2015, 54, 4981−4989